RSC Advances

PAPER

View Article Online
View Journal | View Issue

Cite this: *RSC Adv.*, 2021, **11**, 19890

Graphene/silver-based composites and coating on dead coral for degradation of organic pollution using the Z-scheme mechanism†

Maedeh Nooriha Najafabadi, Hajar Ghanbari * and Rahim Naghizadeh

A high-performance photocatalytic nanocomposite consisting of silver phosphate-based particles with GO and RGO was synthesized by co-precipitation and hydrothermal methods. Ag_3PO_4 was prepared by a co-precipitation method. The as-prepared Ag_3PO_4 nanocomposites were characterized by different analyses. The results demonstrated that the Ag_3PO_4 particles were well dispersed on the graphene-based surfaces. The photocatalytic performance of the GO/RGO/Ag_3PO_4 nanocomposite was evaluated for the photodegradation of methylene blue (MB) under exposure to visible light (xenon lamp $\lambda > 400$ nm). The degradation rate was about 98% in 5 min. The enhancement in photocatalytic performance is attributed to the simultaneous presence of RGO and GO, which show significantly high absorption of organic molecules on the surface of GO/RGO, allowing the effective transfer and separation of photogenerated electrons. In addition, this modified structure can be *in situ* synthesized on dead coral structures that can be used in future real case-studies of the degradation of other organic pollutants. The ingredient of these composites, however, is about 93% Ag_3PO_4.

Received 15th February 2021
Accepted 13th May 2021

DOI: 10.1039/d1ra01239h

rsc.li/rsc-advances

1. Introduction

Nowadays, water treatment is a fundamental global challenge due to the lack of safe drinking water, extensive population growth,[1] and the development of water-polluting industries (*e.g.*, oil refineries, textile and dyestuff factories, hospitals).[2] Biological (viruses, bacteria, and fungi),[3] mineral (nitrate, sulfate, and heavy metal), and organic contaminants (medicinal, dung, dyestuffs, oil, larvicides) are three major pollutants of water. Natural organic matter (NOM) causes an unpleasant odor, taste, and a change in the color of the water; in addition, this wide-ranging family prevents cation removal by forming complex compounds.[4,5]

There are many different methods for removing organic pollutions from water: physical (filtration), chemical (chlorine and ozone disinfection, coagulation, sedimentation, and advanced oxidation processes (AOPs)), and microorganisms-based (bacterial).[5–7] As a subset of AOPs, photocatalysis is an eco-friendly approach for the degradation of organic pollutants in water that is based on the application of clean solar energy.[2,7–11] In this approach, with regard to the exposure of the semiconductor to light with $h\nu \geq E_g$, electrons are excited from the valence band (VB) to the conduction band (CB), while an electron (e^-)–hole (h^+) pair is photogenerated (*i.e.*, a charge carrier). When the charge carriers have arrived at the surface of the photocatalyst, organic materials can be oxidized or reduced, and active superoxide (O_2^-) or hydroxyl radical ($^{\bullet}OH$) and hydrogen peroxide (H_2O_2) are produced.[5,9,12] Among the challenges to this approach is the low efficiency in visible light as well as the recombination of charge carriers. Besides, most semiconductors often have a wide-band gap, which results in activity in the ultraviolet range of light.[5,12,13] Therefore, designing, manipulating, or decorating the semiconductor structure can be targeted to decrease the band gap for activity in the visible light region. Various mechanisms of charge carrier transfer and band structure manipulation routes are as follows: Schottky junctions, Type-II heterojunctions, Z-scheme heterojunctions, and van der Waals heterostructures.[5,12,14] These mechanisms are obtained by coupling two semiconductors or metal complexes, metal doping or noble metal-based plasmonic nanoparticles (Ag, Au, Pt). Although it could be interesting to design a structure based on the collaborative advantages of two or all of these solutions. Among these strategies, Type-II heterojunction and Z-scheme are more effective. Although the Z-scheme heterojunction has the same band structure as a Type-II heterojunction, their charge carrier transfer is different.[14]

Recently, graphene (G), which is semimetallic with zero band gaps, has attracted much attention in improving photocatalysis performance. The properties of graphene include high electrical conductivity, low density, high flexibility, high electron mobility (200 000 $cm^2\ V^{-1}\ s^{-1}$), high specific surface (2600 $m^2\ g^{-1}$), hydrophobicity, and acceptable surface plasmon resonance. Composites

School of Metallurgy & Materials Engineering, Iran University of Science and Technology (IUST), Narmak, Tehran, Iran. E-mail: hajar_ghanbari@iust.ac.ir; Tel: +98 21 73228823

† Electronic supplementary information (ESI) available. See DOI: 10.1039/d1ra01239h

containing graphene can benefit from increased pollution absorption, reduced band gap, higher surface area, limited recombination, and an improved charge carrier migration rate.[15–18] Graphene composites can also increase the capacity of pollutant degradation by enhancing the ultra-wide spectral response.[18–20]

Graphene oxide, a graphene derivative with different properties due to oxygen functional groups,[21] has attracted much attention. Hydrophilicity, resistance to agglomeration in an aqueous medium, and increased surface area compared to RGO are the characteristics we can benefit from in preparing a photocatalytic RGO composite.[22,23] Significantly, the oxygen-containing functionalities and edge defects on the semiconducting graphene oxide (GO) also enable it to be a more intriguing nanomaterial for visible-light-driven photocatalysis.[12]

There have been many studies on the two most commonly used photocatalysts of titanium dioxide and zinc oxide so far;[1] however, the band gap is not applicable in visible light. On the other hand, Ag-based semiconductors are appropriate considering toxicity and possibility of band gap manipulation. Metallic nanoparticles, in particular, silver nanoparticles, have received considerable attention due to their potential in the degradation of organic pollutants (dyes), such as MB, MO, Rhodamine B (RhB), and Rhodamine 6G, and also because of their low toxicity, and strong antimicrobial properties.[24,25] By adjusting the morphology, size, and composition of the plasmonic metals on semiconductors to form a strong surface plasmon resonance, the photocatalytic activity can be improved in the visible light range. Ag-based compounds, such as Ag_3PO_4, Ag_2CO_3, $AgGaO_2$, Ag_2CrO_4, Ag_2S, and Ag_2Se, have been mentioned for this usage.[12,24,26,27] Ag_3PO_4 has a body-centered cubic structure type, and it has an indirect band gap (2.36 eV); it is widely used under visible light.[28] Research using Ag_3PO_4 photocatalysts is reviewed in Table 1. It is worth noting that AgNPs have been used to connect activated GO and Ag_3PO_4.[24] In 2018, Reheman *et al.*[29] for the first time synthesized RGO/Ag_3PO_4 QDs in a one-step reduction process using ultrasonic waves and light with an activity of more than 99% in 10 min. Cui *et al.*[8] conducted a study on Ag_3PO_4/RGO/Ag, which degraded 98% of RhB in 30 min of radiation under visible light. The reduced graphene oxide of this composite plays the role of an electron acceptor to prevent electron–hole recombination.

On the other hand, the hydrothermal method is a versatile one in controlling the degree of GO reduction with regard to the reaction temperature. By increasing the hydrothermal temperature to 180 °C, the graphene oxide would be mostly reduced. However, by applying lower temperatures, the manipulation of a graphene oxide suspension with a combination of RGO and GO is possible.

However, to the best of the writers' knowledge, the simultaneous presence of GO and RGO as a substrate for Ag_3PO_4 nanoparticles has not yet been reported. This combination can present a high surface area for the better dispersion and anchoring of Ag-based nanoparticles on RGO/GO nanosheets, inhibition of RGO agglomeration, and higher electrical conductance of Ag-based/G-based nanocomposites.

In this study, GO and Ag_3PO_4 are proposed for use as semiconductors, while RGO and Ag nanoparticles are the conductors in the Z-scheme and heterojunction mechanism (*i.e.*, a multi-heterojunction) to enhance efficient photocatalytic activity under visible light. The best performance, considering the reduction in the recombination of electrons and holes as well as

Table 1 A brief review comparing research based on Ag_3PO_4 photocatalysts

Photocatalyst	Synthesis method	Target pollutant/volume solution/concentration	Mass photocatalyst (g)	Degradation time (min)/efficiency	Year	References
Ag_3PO_4	Ion-exchange	MB/100 ml/15.3 mg l^{-1}	0.3 g	120/30%	2010	28
GO/Ag_3PO_4/Ag	Precipitation	MO/13.5 ml/20 mg l^{-1}	10 mg	24/95%	2013	30
Ag_3PO_4/Ag				24/78%		
GNs/Ag_3PO_4/Ag	Hydrothermal	MO/100 ml/10 ppm	50 mg	120/71%	2015	31
		Congo red		60/100%		
		RhB		120/85%		
RGO/Ag_3PO_4	Hydrothermal	RhB/50 ml/1 × 10^{-5} mol l^{-1}	20 mg	180/98%	2016	32
Ag_3PO_4	Hydrothermal	RhB/150 ml/1 × 10^{-5} mol l^{-1}	0.15 g	UV light-120/99.55%	2017	33
GO and Ag vacancy in Ag_3PO_4	Precipitation and ultrasonic	RhB/50 ml/6 mg l^{-1}	50 mg	40/98%	2018	34
Ag_3PO_4	Sonochemical and hydrothermal	MB/50 ml/5 mg l^{-1}	50 mg	10/99%	2018	35
		RhB		20/99%		
Ag_3PO_4/g-C_3N_4	Precipitation	Diclofenac/100 ml/10 mg l^{-1}		15/100%	2018	36
Ag_3PO_4	Hydrothermal	Phenol/25 ml/0.21 mmol l^{-1}	125 mg	60/100%	2018	37
GO/Ag_3PO_4 QD	Precipitation and ultrasonic	MB/100 ml/10 ppm	10 mg	5/97.5%	2018	29
Aerogel GO/Ag_3PO_4/Ag	Hydrothermal	MB/200 ml/2 g l^{-1}	0.2 g	60/95.53%	2019	38
P/Ag/Ag_2O/Ag_3PO_4/TiO_2	Sol–gel	RhB/50 ml/2 mg l^{-1}	0/05 g	60/97.1%	2015	39
Ag_3PO_4	Hydrothermal and precipitation	MB/50 ml/10 mg l^{-1}	0.01 g	120/79.4%	2019	40
RGO/Ag_3PO_4	Hydrothermal	MB/100 ml/—	50 mg	15/96.8%	2019	41
		RhB		15/92%		

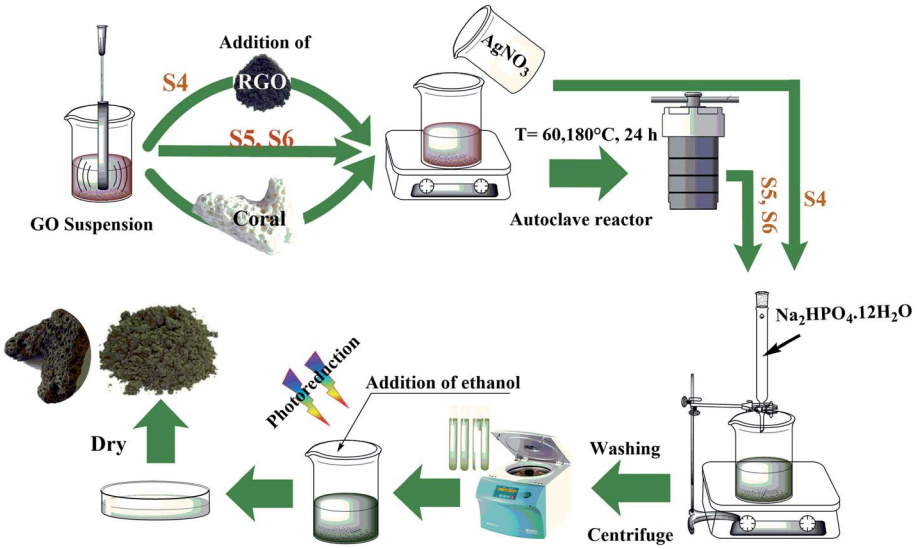

Fig. 1 Schematic steps of composite powder synthesis.

improving the photocatalytic activity, occurred in two samples of RGO/GO/Ag_3PO_4 and GO/Ag_3PO_4 synthesized by a hydrothermal (60 °C for 24 h) method, where the graphene and graphene oxide were present simultaneously.

2. Experimental

2.1. Materials

In order to synthesize graphene oxide, graphite (325 mesh), sulfuric acid (H_2SO_4, 98%), *ortho*-phosphoric acid (H_3PO_4, 85%), hydrochloric acid (HCL, 20%), hydrogen isopropoxide (H_2O_2, 33%), and deionized water (distilled water) were purchased from Iran Persian Chemical Co, Iran. In order to synthesize the composite and test the photocatalytic degradation, potassium permanganate ($KMnO_4$), silver nitrate ($AgNO_3$), disodium hydrogen phosphate dodecahydrate ($Na_2HPO_4 \cdot 12H_2O$), methylene blue ($S_{36}H_{18}ClN_3S$), and ethanol were used in analytical grade from the Merk company (Germany). The reduced graphene oxide employed was research-grade (United Nanotech Innovations Pvt Ltd). In this work, Persian Gulf water corals were used as a substrate for composite coatings.

2.2. GO/RGO/Ag_3PO_4/Ag composite powder synthesis

Graphene oxide was synthesized by Hummers' method[42] (GO1), while GO2 was prepared after an extended period of HCl washing (72 h), compared to GO1 (24 h) in the 1st stage of washing. The composites were prepared by the co-precipitation method. According to Fig. 1 and Table 2, 50 ml (0.25 mg ml^{-1}) of graphene oxide and 0.0125 g of commercial RGO with an RGO : GO ratio of 1 : 1 were dispersed by ultrasonic irradiation for 10 min. Then, 0.5 g of $AgNO_3$ was dissolved in this suspension and stirred on a magnetic stirrer for 12 h. A solution of 0.2 g of $Na_2HPO_4 \cdot 12H_2O$ in 50 ml of deionized water was gradually added to the as-prepared suspension with a burette under dark conditions at room temperature. The collected precipitate was washed with water and then ethanol by centrifuge at 6000 rpm for 2 min. This suspension was placed under a Xe lamp light to perform the reduction process in the presence of ethanol to convert Ag^+ cations to Ag metallic nanoparticles. Finally, the sample was dried in an oven at 65 °C for 3 h. Before adding $Na_2HPO_4 \cdot 12H_2O$, the reduction step in two samples (S5 and S6) was carried out by the hydrothermal method at 60 °C and 180 °C for 24 h. The other two samples (S1 and S2), similar

Table 2 The codes and synthesis methods of the samples

Code of Samples	Samples	Method
RGO	Reduced graphene oxide	Commercial
GO1	Graphene oxide 1	Hummers
GO2	Graphene oxide 2	Hummers
S1	Reduced graphene oxide	Hydrothermal (60 °C)
S2	Reduced graphene oxide	Hydrothermal (180 °C)
S3	Ag_3PO_4	Co-precipitation
S4	RGO/GO1/Ag_3PO_4	Co-precipitation
S5	GO2/Ag_3PO_4/Ag	Hydrothermal (60 °C)–Co-precipitation
S6	GO2/Ag_3PO_4/Ag	Hydrothermal (180 °C)–Co-precipitation

to the S5 and S6 samples, were reduced at 60 °C and 180 °C for 24 h in an autoclave as the case-controls.

2.3. *In situ* coating of GO/Ag_3PO_4 on the coral

First, the coral was put into phosphoric acid for about a few minutes and then washed with deionized water several times (repeatedly). Three irregular coral pieces (~2 × 1 × 1 cm) were dipped in graphene oxide suspension 25 ml (0.5 mg ml^{-1}). Then, silver nitrate solution was added to the suspension and placed in a Teflon-lined autoclave at 60 °C for 12 h. Finally, the corals were dipped in $Na_2HPO_4 \cdot 12H_2O$ solution, set on a shaker for 5 h, and dried in an oven at 200 °C for 2 h. The material ratios used are similar to the ratios used in S5.

2.4. Characterization

The phase structure of the samples was characterized by X-ray Diffraction (XRD) with a general-purpose X-ray diffractometer DRON-8 using CuKα (λ = 0.154 nm) radiation in the 2θ range from 10° to 80°, at 40 kV and 20 mA. Fourier Transform Infrared (FT-IR) spectra were recorded by a Nicolet Avatar 380 spectrometer. Raman spectroscopy was applied with a Teksan (Takram P50C0R10) with a DPSS Nd:YAG laser, laser wavelength = 532 nm, laser power = 100 mW, and spectral resolution of 10 cm^{-1}. UV-vis diffuse reflectance spectra (UV-vis DRS) were accomplished with a Shimadzu instrument. The UV-vis spectra were obtained with a T80 UV-vis spectrometer PG Instrument to calculate the amount of degradation of organic pollutants. Field Emission Scanning Electron Microscopy (FE-SEM) images were taken with a MIRA3TESCAN-AMU at 3–30 kV voltage. The photoluminescence (PL) spectra were also analyzed with a Varian Cary Eclipse fluorescence spectrophotometer at an excitation wavelength of 315 nm.

2.5. Photocatalytic activity

The photocatalytic activity was evaluated by measuring the decomposition rate of MB in an aqueous solution under light from a xenon lamp. The inside of the lamp housing system is covered with aluminum foil and consists of two xenon lamps of 100 W (λ > 400 nm), located at a distance of about 20 cm from each other. Also, there is a cooling system consisting of two fans and water circulation in the lamp housing. A picture of the lamp housing system is shown in Fig. S1.† The as-prepared powder (50 mg) was added to 50 ml of MB solution (20 ppm). After stirring for 30 min to complete the adsorption–desorption equilibrium in a dark environment, periodic sampling was undertaken during exposure to visible light at specific time intervals.

3. Results and discussion

3.1. Phase characterization

In Fig. 2a, the results of phase identification and the relative amount of GO2 reduction at two hydrothermal temperatures of 60 and 180 °C (RGO-60 and RGO-180) are compared. In Fig. 2b, the XRD patterns of the as-prepared samples by co-precipitation (S3 and S4) and hydrothermal–co-precipitation methods at 60 °C and 180 °C (S5 and S6) are shown. The Ag_3PO_4 phase is identified in all samples at 2θ of 21.1°, 30.0°, 30.5°, 36.8°, 38.4°, 48.0°, 52.9°, 55.3°, 57.5°, 61.9°, and 72.1°, which is consistent with previous research, according to JCPDS NO:06-0505.[8,29,31,34,43] Regarding the accuracy of XRD analysis, the Ag peak was only detected in S6. However, no peaks belonging to G or GO phases were observed in S3, S4, S5, or S6. These observations can be justified by (i) the low weight percentage (% wt) of G(GO) and Ag, (ii) the increased interlayer distance between the graphene oxide sheets due to the intercalation of Ag_3PO_4 and Ag nanoparticles between the layers of G and GO, (iii) as well as the decrease in the amount of Ag nanoparticles.[31] The crystallite size of Ag_3PO_4 was calculated with the Debye–Scherrer equation,[44] using eqn (1).

$$L = 0.9\lambda/\mathrm{FWHM}\cos\theta \quad (1)$$

where λ is the X-ray wavelength (1.5406 Å), FWHM is the full width at half maximum, and θ is the diffraction angle. The

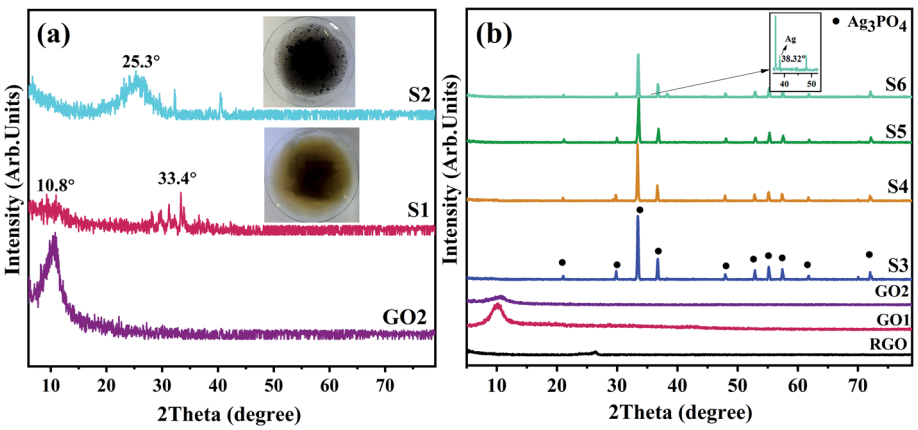

Fig. 2 XRD patterns of synthesized samples: (a) GO2 sample and reduced GO2 in two different hydrothermal conditions: from bottom to top GO2, S1 and S2, (b) from bottom to top RGO, two graphene oxide samples (GO1 and GO2), as-prepared composite by co-precipitation (S3, S4) and by hydrothermal–co-precipitation methods (S5, S6).

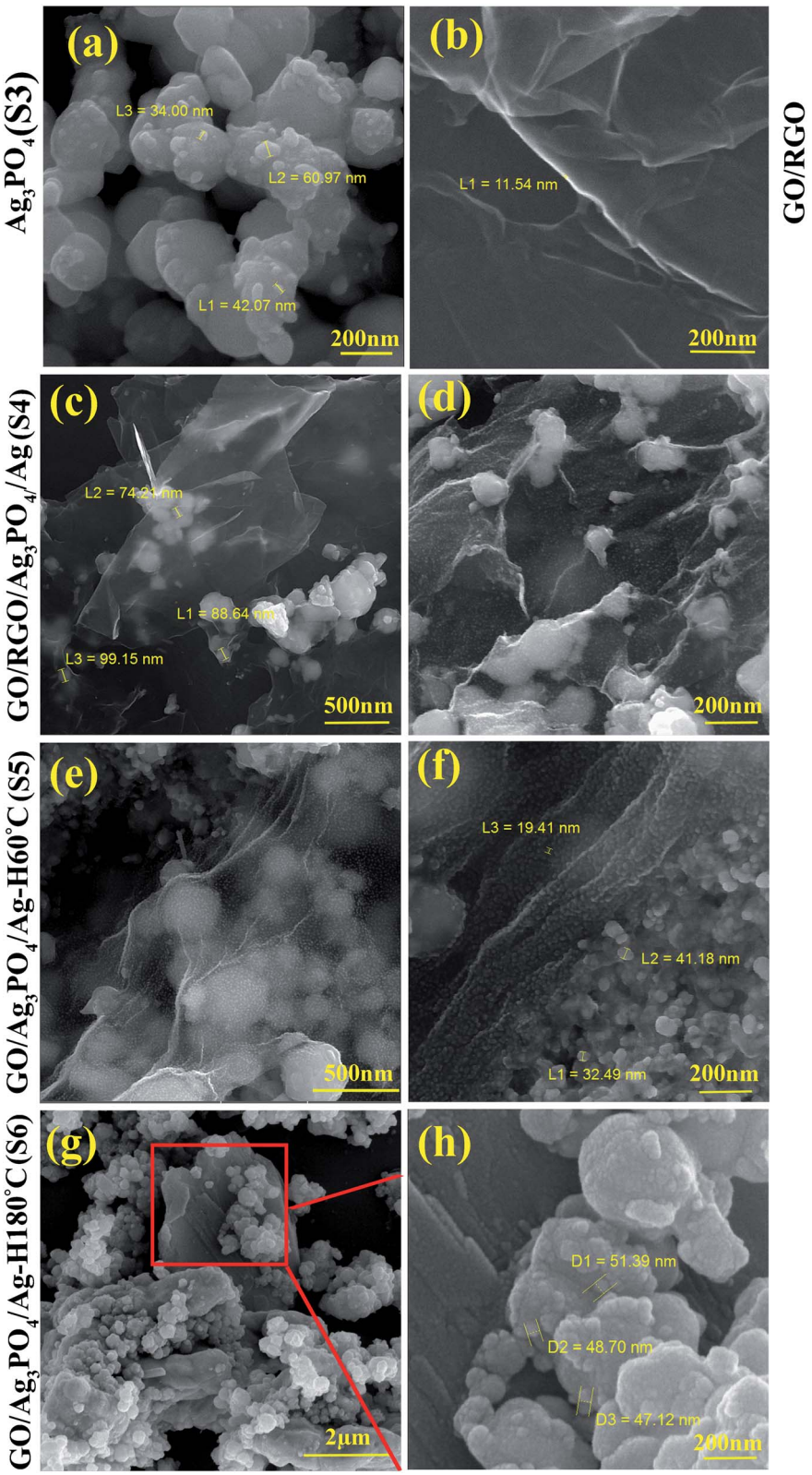

Fig. 3 FE-SEM images of (a) S3, (b) GO/RGO at 150k× magnification, (c) and (d) S4 at 75 and 150k×, (e) and (f) S5 at 150k× and (g) and (h) S6 at 25 and 150k× magnification.

average crystallite size of pure Ag_3PO_4 (S3) is about 51 nm, while these indices are 41 and 45 nm in GO/Ag_3PO_4 prepared with the hydrothermal processes at 60 °C (S5) and 180 °C (S6), respectively, and 50 nm in RGO/GO/Ag_3PO_4/Ag (S4). Considering the particle size of Ag_3PO_4 synthesized in the different processes, GO and RGO play roles in the decrease in particle size

of Ag_3PO_4 by providing more surface for the heterogeneous nucleation of the phosphate phase. In addition to the surface area, the surface charge is also essential in nucleation and growth. The addition of commercial RGO in S4 is effective in the Z-scheme mechanism. However, the lower amount of negative charges on the surface of commercial RGO attenuates the nucleation and growth of Ag_3PO_4 embryos compared to the as-synthesized GO used in S4 and S5, resulting in the larger particle size of Ag_3PO_4 in S4.

3.2. Field emission scanning electron microscopy (FE-SEM)

FE-SEM was employed to investigate the particle distribution and morphology of the synthesized particles on the sheets in the as-prepared samples. In Fig. 3, FE-SEM images of (a) S3, (b) GO/RGO, (c and d) S4, (e and f) S5, and (g and h) S6 are highlighted. The particle size distributions of Ag_3PO_4 prepared without GO or RGO, shown in Fig. 3a, are in the range of 30–80 nm. Fig. 3b highlights the FE-SEM images of mixed and dispersed GO and RGO before the formation and decoration of Ag_3PO_4 (Ag), showing a layered structure of less than ~10 nm thickness. A comparison between the composites prepared with co-precipitation (S4) and hydrothermal/co-precipitation/(60 and 180 °C) shows that a broader particle size distribution of Ag_3PO_4 (Ag) occurred in S4 and S5 compared to S6, which could originate from the presence of GO in the latter samples. However, Ag_3PO_4 nanoparticles with a particle size of less than 100 nm were detected in all as-prepared composites.

The application of GO in the synthesis step (S4, S5, S6) promotes the controlled nucleation and growth of Ag_3PO_4. The complete reduction of GO in S6, caused by the higher temperature of the hydrothermal process, reduces the oxide and hydroxyl groups on the surface of GO (Fig. 2a), thus forcing the Ag ions to partially precipitate as Ag metallic particles on the surface of the graphene layers, as confirmed by the XRD results shown in Fig. 2b (S6). On the other hand, simultaneous restacking and agglomeration of the as-reduced RGO would take place in S6. In all four samples, the Ag ions in the solution would react with phosphate ions in the subsequent co-precipitation step to form Ag_3PO_4

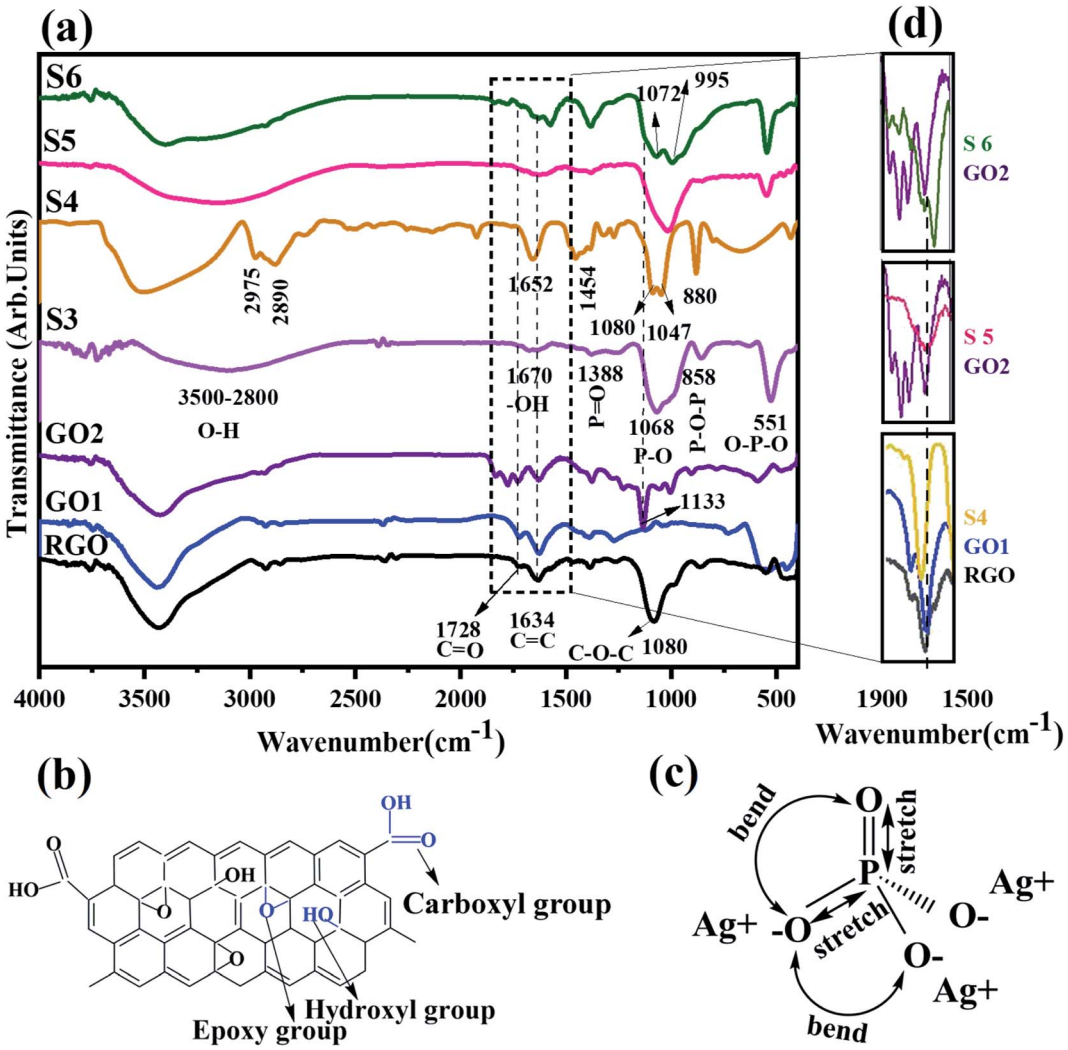

Fig. 4 (a) FT-IR spectra of as-prepared RGO, GO1, GO2, S3 (pure Ag_3PO_4), S4 (RGO/GO/Ag_3PO_4/Ag), S5 and S6 (GO/Ag_3PO_4 hydrothermal at 60 and 180 °C); (b) and (c) the schematic bands of graphene oxide and Ag_3PO_4, respectively; (d) the selected part at 1500–1900 cm^{-1}, redrawn according to the GO/RGO used in each composite.

nanoparticles. Although, in S4 and S5 samples, the formation of Ag_3PO_4 in the co-precipitation step would take place in a more homogenized manner due to the anchored Ag ions on the not-reduced GO surfaces.

3.3. Fourier-transform infrared spectroscopy (FT-IR)

The characterization of functional groups and bands was carried out by FT-IR spectroscopy analysis. Fig. 4a shows the FTIR spectra of the as-prepared samples according to Table 2. FT-IR spectra of RGO, GO1, and GO2 show five main peaks at 3600–3400, 1080, 1133, 1634, and 1728 cm^{-1}. A broad and strong peak at 3600–3300 cm^{-1} is ascribed to the O–H stretching vibration of the hydroxyl group,[29,45] while 1080 and 1133 cm^{-1} display epoxy group stretching vibration in C–O–C (alkoxy or epoxy group) over the basal plane in RGO and GO2. The stretching vibration in C=C of the un-oxidized graphitic domain on the basal plane or of the graphene sheets and C=O (COOH) in carbonyl groups on the edge of the graphene oxide sheets are displayed at 1634 cm^{-1} and 1728 cm^{-1},[8,16,29,34,45,46] respectively. There are some sub-absorption peaks at the wavenumbers of 1278, 1388, 2377, and 2931 cm^{-1}, which were ascribed to C–O–C, the bending vibration of O–H,[8,16,46] CO_2 (O–C=O),[16] and the stretching vibration of C–H, respectively. Fig. 4b shows the schematic structure of graphene (oxide) and related functional groups.

The absorption bands at 540, 858, 1066, 1388, and 1670 cm^{-1} were assigned to bending of P=O–P, bending of P–O–P, stretching of P–O, stretching of P=O (schematically shown in Fig. 4c)[36] and –OH vibration on Ag_3PO_4, respectively.[32,33] This –OH band is due to the physical absorption of water on pure Ag_3PO_4.[7,33] In Fig. 4d, the selected parts of Fig. 4a at 1500–1900 cm^{-1} are redrawn according to the shift in the C=O bonding peak. The peak shift of C=O in the S5 and S6 composites (hydrothermal method) relative to the initially applied graphene oxide towards a lower wavenumber confirms the charge interaction between rGO and Ag_3PO_4, which agrees well with previously reported work.[8,29,30]

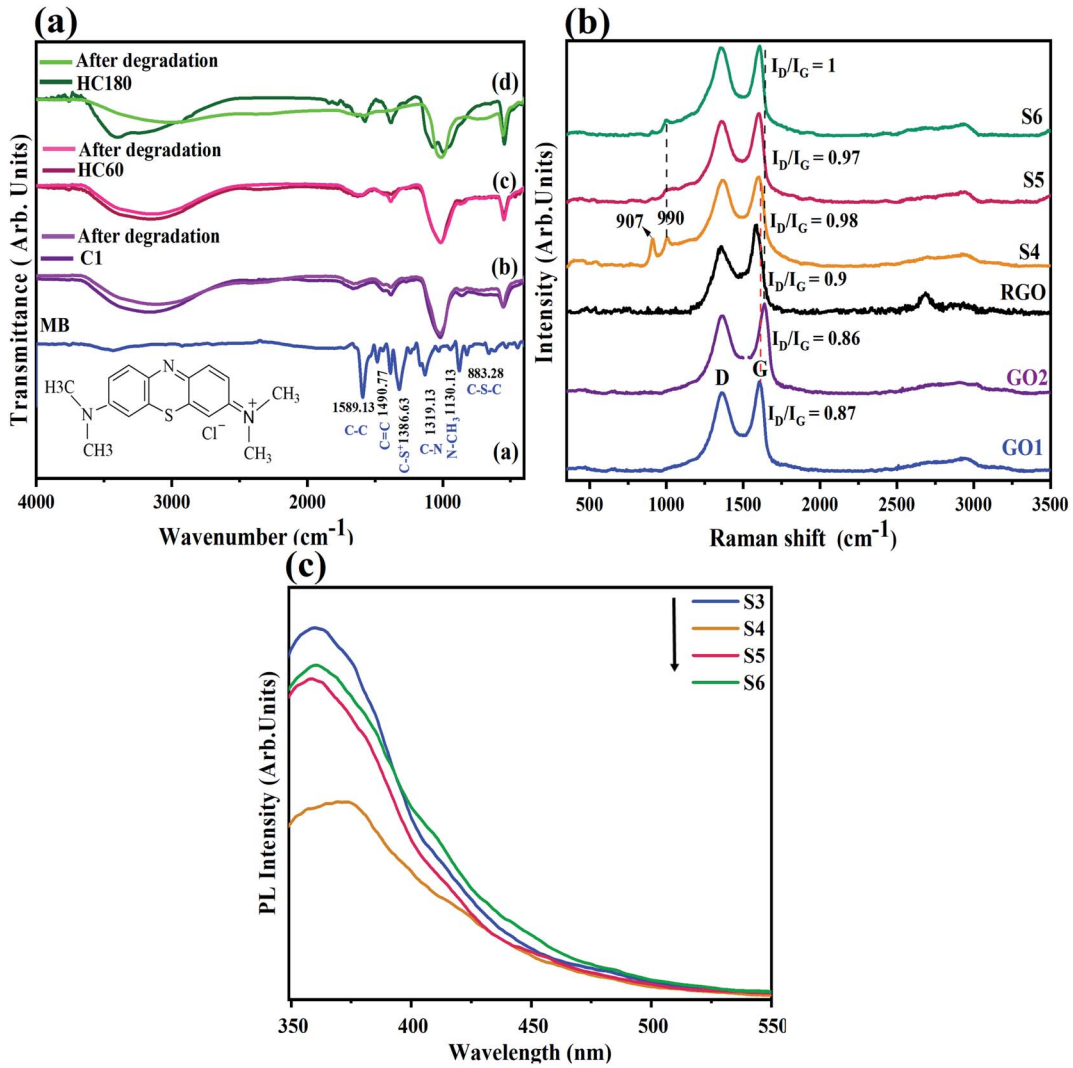

Fig. 5 (a) FTIR spectra of MB, S3, S5, and S6 before and after irradiation with visible light. (b) Raman spectroscopy of different photocatalysts: S3, S4, S5, and S6. (c) PL spectra for different photocatalysts: S3, S4, S5, and S6.

On the other hand, in S4, S5, and S6 composite samples, the C=O peak at 1728 cm^{-1} in graphene oxide samples disappears due to the progress of reduction in graphene oxide. The overlap of P–O (Ag_3PO_4) and C–O–C (GO) produces a branched peak in S4 and S6 at about 995–1072 cm^{-1} and 1047–1080 cm^{-1}, respectively. The first and the second bands are attributed to P–O and C–O–C bands, respectively. This result confirms the formation of composites.[25,32]

In order to verify the stability of the photocatalytic process in pure Ag_3PO_4 as well as the composites before and after degradation of MB, the related FT-IR spectra are compared in Fig. 5a. The results indicate that the samples remained unchanged after the photocatalytic activity in S5 and S3, while in S6, the structure changed after the photocatalytic process.

3.4. Raman spectroscopy

Raman spectroscopy is one of the most critical methods for studying carbon materials such as graphite, graphene, *etc.* Fig. 5b shows Raman spectra of GO1, GO2, RGO, S4, S5, and S6 powders. In graphene structures, two peaks nominated as the D-band (attributed to the disorder-induced phonon mode of the vibrations of sp^3 atoms of carbon) and G-band (related to the first-order scattering of the E_{2g} mode in the sp^2 carbon lattice in the graphitic domains) are the most dominant. The G-bands in GO1 and GO2 are located at 1608 cm^{-1} and 1630 cm^{-1}, respectively. The G-band in GO2 is shifted toward a higher wavenumber, which can be interpreted by the higher degree of oxidation in this sample,[47] consistent with the FTIR results in Fig. 4a. There was no significant change in the D-band position. Generally, the D to G-band (I_D/I_G) intensity ratio can determine the defects and disorder in graphene sheets. In GO1 and GO2, I_D/I_G is 0.87 and 0.86, respectively, which reflects a minor improvement in the reduction step, which is observed in mainly sp^2 amorphous carbon materials.[47,48] This ratio increases in all composites (0.98, 0.97, and 1 in S4, S5, and S6, respectively). The increase in disorder arises from decorating of Ag_3PO_4 on the GO and RGO sheets.[8,30] By comparing the I_D/I_G of the composites, the highest value was found in S6 while the lowest value was measured in the S5 sample, which is related to the lower degree of reduction in S5, as shown in the XRD patterns in Fig. 2a. This result also implies the partial reduction of GO at 60 °C. The G-bands in S4, S5, and S6 found at *ca.* 1597, 1603, and 1603 cm^{-1} reflect a red-shift compared to the primary graphene oxides that emerge from the interaction between GO and Ag/Ag_3PO_4, where the latter species donate electrons while the GO sheets accept electrons.[30,49] It is worth noting that the bands centered at 990 and 903 cm^{-1} correspond to the asymmetric stretching vibration of P–O–P bonding.[50]

3.5. Photoluminescence (PL)

One of the considerable and effective challenges for photocatalytic activity is to conserve charge separation. The

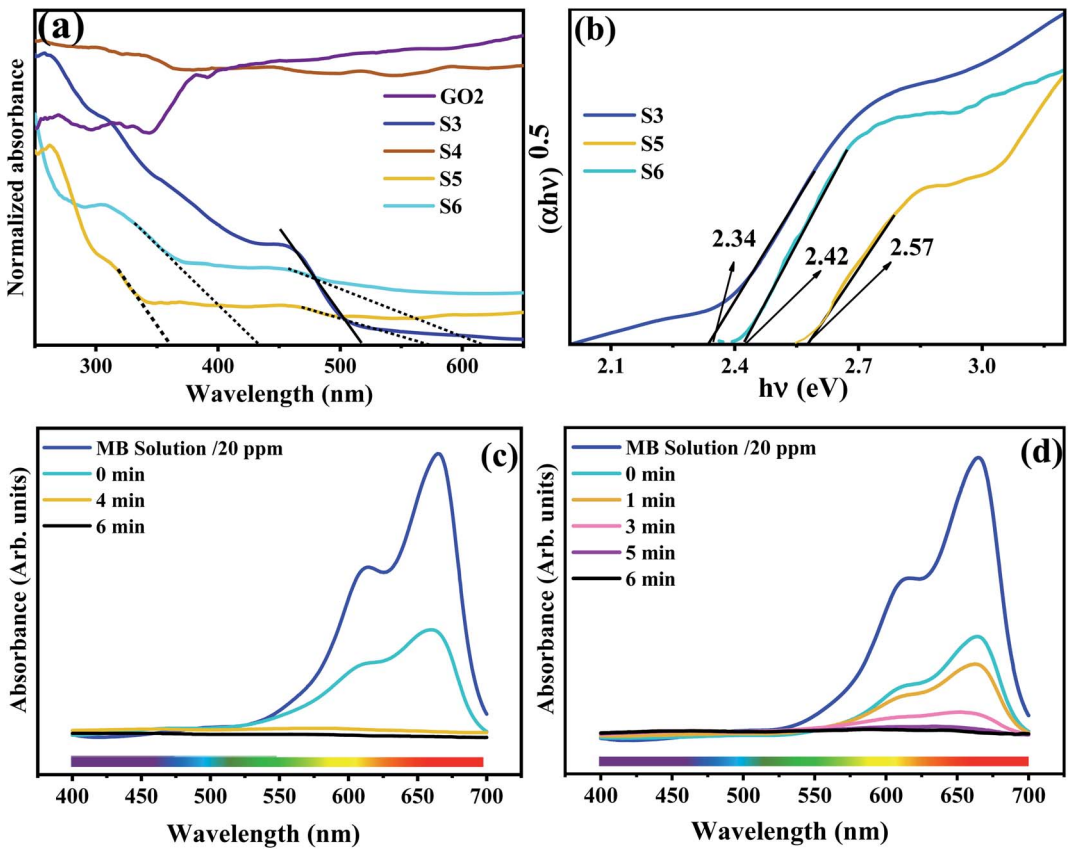

Fig. 6 (a) UV-vis DRS absorption spectra, (b) calculated band gap energies of 2.34, 2.42, and 2.57 eV for S3, S5, and S6, respectively. UV-visible absorption spectra of MB by photocatalyst in (c) S3 and (d) S6.

luminescence spectra of the as-prepared samples are given in Fig. 5c under an excitation wavelength of 315 nm. This wavelength has already been suggested to excite electrons.[25] The lower luminescence intensity implies a lower recombination rate of electron–hole pairs and a prior photocatalytic activity. The luminescence intensity is due to the return of electrons from the conduction band to the valence band and recombination with holes after electron excitation by the light. The PL emission intensity is reduced, where S4 < S5 < S6 < S3. The lower intensity in the S4 and S5 samples is probably due to the simultaneous presence of RGO and GO in the as-prepared structures.

The charge transfer followed by the reduced recombination would be improved with silver on partial RGO structures,[8] because the Ag nanoparticles are well dispersed on the GO substrates and, at the same time, conductive dispersed RGO would increase the charge transfer and prevent the electron–hole recombination.

3.6. UV-vis DRS analysis

As reported, the optical property of the semiconductor is the crucial factor that determines the photocatalytic performance. The UV-Vis DRS diagrams of GO2, S3, S4, S5, and S6 dried powder are shown in Fig. 6a. The absorbance wavelength in S3 (Ag_3PO_4) is about 520 nm. With regard to the S5 and S6 samples, two absorbance wavelengths can be seen. In S5, there are two peaks at about 360 in the UV and visible light range, respectively. However, the distinguished absorbance wavelengths in S6, similar to S5, exist in 430 and continuous absorption in 520–700 nm. It seems that the absorbance in these two samples is more substantial (500–700 nm) than for S3 due to the presence of RGO or the simultaneous presence of GO and RGO, as previously reported.[8,31,43] However, high absorption in a broad band is a typical feature of carbon-based composites. Estimations of band gap energy (E_g) reported for S3, S5, and S6 are shown in Fig. 6b. The semiconductor band gap can be obtained from the Kubelka–Munk function, using eqn (2).

$$(\alpha h\nu) = A(h\nu - E_g)^n \quad (2)$$

where α, A, n, $h\nu$, and E_g are the diffuse reflection absorption coefficient, proportionality constant, a coefficient that depends on the type of electronic transition, photon energy, and the band gap energy, respectively.[51] The electron transition type for as-prepared Ag_3PO_4 powder is indirect, and the proposed n is equal to 2.[50,52] The calculated band gap values for S3, S5, and S6 were 2.34, 2.57, and 2.42 eV, respectively. It seems that the less accomplished reduction of GO with the synergetic effect of the smaller crystallite size of Ag_3PO_4 in S5 could be the reason for the more significant band gap in this sample.[7,51,53]

3.7. Photocatalytic performance

The effect of RGO and GO on the photocatalytic activity of Ag_3PO_4 in S3, S4, S5, and S6 was evaluated. Fig. 6c and

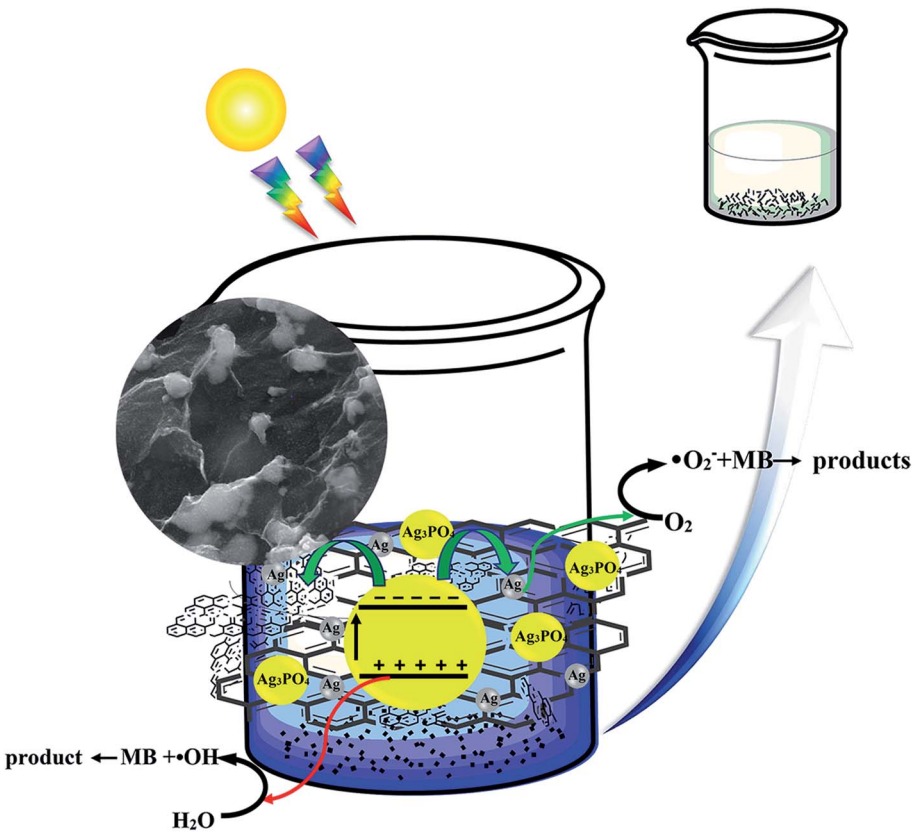

Fig. 7 Schematic of the proposed photocatalysis and degradation mechanism of MB on the surface of the composites (RGO/GO/Ag_3PO_4/Ag).

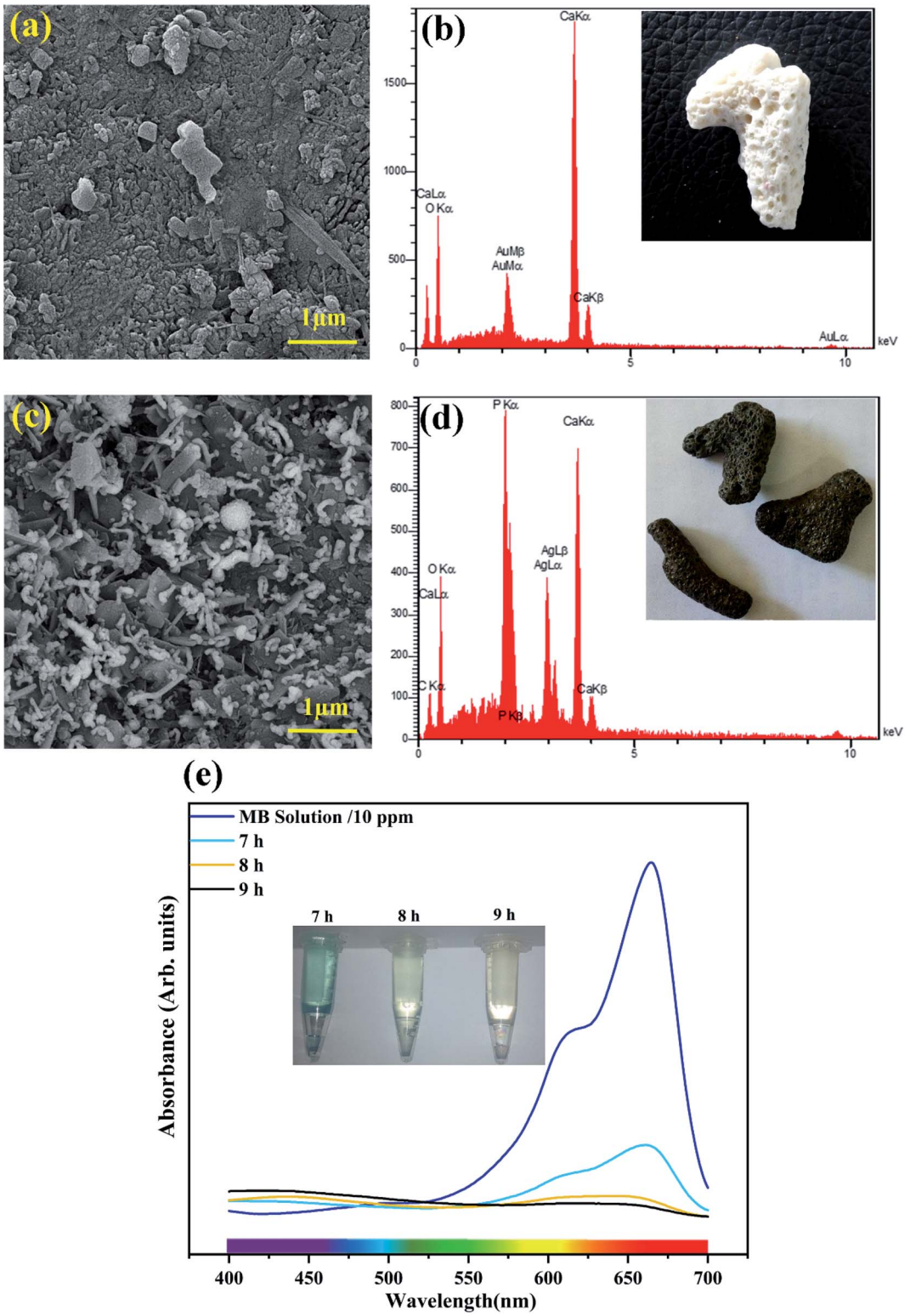

Fig. 8 FE-SEM images of (a) pure coral and (c) coral coated with GO/Ag_3PO_4; EDS of (b) pure coral and (d) coral coated with GO/Ag_3PO_4; (e) UV-visible absorption spectra of MB photocatalyzed by coral coated with GO/Ag_3PO_4.

d represent the absorption spectra of MB in S3 and S6. However, the photocatalytic activity of S4 cannot be scanned because of the very rapid and high absorption of MB on the surface of this sample so that no real degradation took place due to the electron–hole generation by photocatalysts. Therefore, degradation under exposure to light is impossible, although the change in the color from green to black confirms the degradation of MB (Fig. S2†). Strong adsorption of cationic dye MB in S3

under dark conditions can be related to positive–negative charge attraction between the Ag_3PO_4 surface and MB molecules, respectively, due to the presence of oxygen vacancies.[54,55]

In all cases, absorption and degradation took less than 5 min.

The percentage of decolorization of MB was calculated using eqn (3).

$$\eta\ (\%) = (C_0 - C_t)/C_0 \times 100 \quad (3)$$

where C_0 and C_t are the initial and residual concentrations of MB in the solution. More than 98% of the MB contaminant was removed from the water by S3 and S6. The results are shown in Fig. 6c and d. High absorption can accelerate the degradation process.

3.8. Proposed mechanism

A possible degradation mechanism based upon the above experimental discussion is proposed in Fig. 7. When the RGO/GO/Ag_3PO_4/Ag photocatalyst was exposed to irradiation from xenon lamp light, charge carriers (e^-/h^+) were photogenerated. The electrons in the VB were photoexcited to the CB in the two semiconductors present: Ag_3PO_4 and GO, while the holes remained in the VB. The e^-/h^+ can transfer to the surface to be involved in the degradation process. However, not all the e^-/h^+ can move to the surface and some of them are recombined in the bulk of the semiconductors. When e^-/h^+ reach the surface, they may be recombined. The conductive Ag nanoparticles and RGO nanosheets, as a mediator, can play an intensely critical role in decreasing the recombination process. Then, transferred e^-/h^+ participate in the oxidation and reduction process with regard to the MB degradation. Under irradiation, the e^-/h^+ can react at the interface with water and oxygen to produce reactive oxygen species such as hydroxyl radicals ($^{\bullet}OH$) and superoxide radical anions (O^{2-}) through oxidation or reduction reactions, respectively.[12,43]

3.9. Coral coating with photocatalytic suspension

According to the FE-SEM results in Fig. 8a and c, related to uncoated and coated coral, respectively, worm-shaped particles of silver phosphates are uniformly formed *in situ*. The presence of Ag and P elements in Fig. 8d confirms that the formed particles contain A and P-based composition(s).

In Fig. 8e, UV-vis absorption spectra of MB on the coated coral with photocatalytic suspension are shown. The trend of reduced intensities over time displays the degradation of MB, like that mentioned before on prepared powder, confirming the conserved photocatalytic effect in *in situ* synthesized Ag_3PO_4–RG coatings. Interestingly, the coral coated with photocatalytic composite degrades MB in natural light (indirect radiation by sunlight) in about 9 h (Fig. 8e), unlike the other samples analyzed in xenon light. It is worth noting that exposure to direct sunlight probably reduces the time for removal.

The yield of Ag_3PO_4 QD/RGO to degrade 100 ml MB solution (10 ppm) was reported to be 97.46% for 5 min,[29] while in this work, the simultaneous presence of Ag_3PO_4 and GO would increase the efficiency of the photocatalyst by nearly 2% under similar conditions. Here, the volume and concentration of the solution used are 50 ml and 20 ppm, respectively. The partial presence of GO and RGO as the substrate for the Ag_3PO_4 and Ag particles with regard to the Z-scheme mechanism is proposed to be the reason for the improved performance. This composite shows the potential of an *in situ* preparation as a coating on the dead coral structures.

Investigation on the photocatalytic results of the silver–graphene-based composites shows that the proposed composites present prior photocatalytic activity compared to other similar structures. Cui *et al.* synthesized a comparable Ag_3PO_4/RGO/Ag composite, in which Rhodamine B degrades in 30 min.[8] Degradation of MB by unknown concentration was reported to be 96.8% in 15 min using Ag_3PO_4/PDA (polydopamine)/RGO.[41] The Ag_3PO_4/GO photocatalytic composite powder prepared by the co-precipitation method was reported to degrade about 98% of Rhodamine B in 40 min;[34] however, in this work, the GO/RGO/Ag_3PO_4 composite can degrade three times more concentrated MB in a shorter time (about 5 min).

4. Conclusion

In summary, we have successfully synthesized Ag_3PO_4 and Ag-decorated RGO and GO/RGO photocatalysts. The obtained RGO/GO/Ag_3PO_4/Ag nanocomposites exhibited improved degradation of MB compared with RGO/Ag_3PO_4/Ag under simulated solar light irradiation. The enhancement in photocatalytic activity on GO/RGO compared to GO can be attributed to the high surface area of the composites and the effective transfer and separation of photogenerated electrons and holes by the GO nanosheets. We also showed that RGO and GO in GO/RGO/Ag_3PO_4/Ag would increase the photocatalyst efficiency. In this work, we have tried to modify the composition of a graphene–silver-based structure based on the Z-scheme mechanism while maintaining the high surface area for the uniform deposition of silver-based particles to improve the MB degradation by the photocatalyst in visible light. However, this modified structure can be synthesized *in situ* on dead coral structures that can be used in future real case-studies in the degradation of other organic pollutants.

Conflicts of interest

There are no conflicts to declare.

References

1 B. Liu, Y. Fang, Z. Li and S. Xu, *J. Nanosci. Nanotechnol.*, 2015, **15**, 889–920.
2 M. Taghdiri, *Int. J. Photoenergy*, 2017, **2017**, 8575096.
3 V. Etacheri, C. Di Valentin, J. Schneider, D. Bahnemann and S. C. Pillai, *J. Photochem. Photobiol., C*, 2015, **25**, 1–29.
4 J. Adusei-Gyamfi, B. Ouddane, L. Rietveld, J.-P. Cornard and J. Criquet, *Water Res.*, 2019, **160**, 130–147.
5 M. Lu, *Photocatalysis and water purification: from fundamentals to recent applications*, John Wiley & Sons, 2013.

6 A. Houas, H. Lachheb, M. Ksibi, E. Elaloui, C. Guillard and J.-M. Herrmann, *Appl. Catal., B*, 2001, **31**, 145–157.
7 R. Dhanabal, A. Chithambararaj, S. Velmathi and A. C. Bose, *J. Environ. Chem. Eng.*, 2015, **3**, 1872–1881.
8 C. Cui, Y. Wang, D. Liang, W. Cui, H. Hu, B. Lu, S. Xu, X. Li, C. Wang and Y. Yang, *Appl. Catal., B*, 2014, **158**, 150–160.
9 J. Wen, J. Xie, X. Chen and X. Li, *Appl. Surf. Sci.*, 2017, **391**, 72–123.
10 C. A. Martinez-Huitle, M. A. Rodrigo, I. Sires and O. Scialdone, *Chem. Rev.*, 2015, **115**, 13362–13407.
11 R. Andreozzi, V. Caprio, A. Insola and R. Marotta, *Catal. Today*, 1999, **53**, 51–59.
12 X. Li, R. Shen, S. Ma, X. Chen and J. Xie, *Appl. Surf. Sci.*, 2018, **430**, 53–107.
13 D. Xu, S. Cao, J. Zhang, B. Cheng and J. Yu, *Beilstein J. Nanotechnol.*, 2014, **5**, 658–666.
14 Q. Xu, L. Zhang, J. Yu, S. Wageh, A. A. Al-Ghamdi and M. Jaroniec, *Mater. Today*, 2018, **21**, 1042–1063.
15 F. Kusmartsev, W. Wu, M. Pierpoint and K. Yung, *Application of graphene within optoelectronic devices and transistors*, ed. P. Misra, Springer, 2015, pp. 191–221.
16 C.-M. Chen, *Surface chemistry and macroscopic assembly of graphene for application in energy storage*, Springer, Berlin, Heidelberg, 2015.
17 J. Zhao, L. Liu and F. Li, *Graphene oxide: physics and applications*, Springer, Verlag, Berlin, Heidelberg, 2015.
18 H. Heo, S. Lee and S. Kim, *Carbon*, 2019, **154**, 42–47.
19 Y. Fan, C. Guo, Z. Zhu, W. Xu, F. Wu, X. Yuan and S. Qin, *Sci. Rep.*, 2018, **8**, 1–8.
20 F. Xia, H. Wang, D. Xiao, M. Dubey and A. Ramasubramaniam, *Nat. Photonics*, 2014, **8**, 899–907.
21 M. Inagaki and F. Kang, *J. Mater. Chem. A*, 2014, **2**, 13193–13206.
22 J. Guerrero-Contreras and F. Caballero-Briones, *Mater. Chem. Phys.*, 2015, **153**, 209–220.
23 S. Syama and P. Mohanan, *Nano-Micro Lett.*, 2019, **11**, 6.
24 M. Griffith, K. Udekwu, S. Gkotzis, T. Mah and E. Alarcon, *Silver nanoparticle applications: In the fabrication and design of medical and biosensing devices*, Springer, Switzerland, 2015.
25 A. Samal, D. Das, K. Nanda, B. Mishra, J. Das and A. Dash, *Chem.–Asian J.*, 2016, **11**, 584–595.
26 S. Song, B. Cheng, N. Wu, A. Meng, S. Cao and J. Yu, *Appl. Catal., B*, 2016, **181**, 71–78.
27 Y. Wan, C. Liang, Y. Xia, W. Huang and Z. Li, *Appl. Surf. Sci.*, 2017, **396**, 48–57.
28 Z. Yi, J. Ye, N. Kikugawa, T. Kako, S. Ouyang, H. Stuart-Williams, H. Yang, J. Cao, W. Luo and Z. Li, *Nat. Mater.*, 2010, **9**, 559–564.
29 A. Reheman, Y. Tursun, T. Dilinuer, M. Halidan, K. Kadeer and A. Abulizi, *Nanoscale Res. Lett.*, 2018, **13**, 70.
30 M. Zhu, P. Chen and M. Liu, *Chin. Sci. Bull.*, 2013, **58**, 84–91.
31 R. Jiang, H. Y. Zhu, J. B. Li, F. Q. Fu, J. Yao, X. X. Liang, R. Q. Guo and G. M. Zeng, *J. Iran. Chem. Soc.*, 2016, **13**, 1167–1174.
32 L. Wang and Y. Zhou, *Fullerenes, Nanotubes, Carbon Nanostruct.*, 2016, **24**, 588–593.
33 S. Krungchanuchat, N. Ekthammathat, A. Phuruangrat, S. Thongtem and T. Thongtem, *Mater. Lett.*, 2017, **201**, 58–61.
34 R. Liu, H. Li, L. Duan, H. Shen, Q. Zhang and X. Zhao, *Appl. Surf. Sci.*, 2018, **462**, 263–269.
35 C. S. Tseng, T. Wu and Y. W. Lin, *Materials*, 2018, **11**, 708.
36 W. Zhang, L. Zhou, J. Shi and H. Deng, *Catalysts*, 2018, **8**, 45.
37 J. Zwara, E. Grabowska, T. Klimczuk, W. Lisowski and A. Zaleska-Medynska, *J. Photochem. Photobiol., A*, 2018, **367**, 240–252.
38 M. Deng and Y. Huang, *Ceram. Int.*, 2020, **46**, 2565–2570.
39 X. Hu, Q. Zhu, X. Wang, N. Kawazoe and Y. Yang, *J. Mater. Chem. A*, 2015, **3**, 17858–17865.
40 J. Niu, Z. Zhang, K. Wang, W. Shi and X. Yu, *IOP Conf. Ser.: Earth Environ. Sci.*, 2019, **344**, 012069.
41 R. Zhang, T. Zhang, Y. Cai, X. Zhu, Q. Han, Y. Li and Y. Liu, *J. Inorg. Organomet. Polym. Mater.*, 2020, **30**, 543–553.
42 T. Nematian, A. Shakeri, Z. Salehi and A. A. Saboury, *Biotechnol. Biofuels*, 2020, **13**, 1–15.
43 L.-L. Qu, N. Wang, Y.-Y. Li, D.-D. Bao, G.-H. Yang and H.-T. Li, *J. Mater. Sci.*, 2017, **52**, 8311–8320.
44 A. Monshi, M. R. Foroughi and M. R. Monshi, *World J. Nano Sci. Eng.*, 2012, **2**, 154–160.
45 G. Pavoski, T. Maraschin, F. d. C. Fim, N. M. Balzaretti, G. B. Galland, C. S. Moura and N. R. d. S. Basso, *Mater. Res.*, 2017, **20**, 53–61.
46 T. Parandhaman and S. K. Das, *Biomater. Sci.*, 2018, **6**, 3356–3372.
47 K. Krishnamoorthy, M. Veerapandian, K. Yun and S.-J. Kim, *Carbon*, 2013, **53**, 38–49.
48 I. Childres, L. A. Jauregui, W. Park, H. Cao and Y. P. Chen, *New Dev. Photon Mater. Res.*, 2013, **1**, 1–20.
49 M. Zhu, P. Chen and M. Liu, *ACS Nano*, 2011, **5**, 4529–4536.
50 G. Botelho, J. C. Sczancoski, J. Andres, L. Gracia and E. Longo, *J. Phys. Chem. C*, 2015, **119**, 6293–6306.
51 X. Guan, J. Shi and L. Guo, *Int. J. Hydrogen Energy*, 2013, **38**, 11870–11877.
52 A. Escobedo-Morales, I. Ruiz-López, M. d. Ruiz-Peralta, L. Tepech-Carrillo, M. Sánchez-Cantú and J. Moreno-Orea, *Heliyon*, 2019, **5**, e01505.
53 P. Sehrawat, S. Islam, P. Mishra and S. Ahmad, *Sci. Rep.*, 2018, **8**, 1–13.
54 X. Liu, J. Xu, Z. Ni, R. Wang, J. You and R. Guo, *Chem. Eng. J.*, 2019, **356**, 22–33.
55 M. Al Kausor, S. S. Gupta and D. Chakrabortty, *J. Saudi Chem. Soc.*, 2020, **24**, 20–41.